Three scale modeling of the behavior of a 16MND5-A508 bainitic steel: Stress distribution at low temperatures

Raphaël Pesci, Karim Inal, Renaud Masson

Three scale modeling of the behavior of a 16MND5-A508 bainitic steel: Stress distribution at low temperatures

Raphaël Pesci [a,*], Karim Inal [b], Renaud Masson [c,1]

[a] LPMM UMR CNRS 7554, Ecole Nationale Supérieure d'Arts et Métiers, 4, avenue Augustin Fresnel, Technopôle Metz 2000, 57078 Metz cedex 3, France
[b] ENSMSE CMP-PS2, Quartier Saint Pierre, Avenue des Anémones, 13120 Gardanne, France
[c] Electricité De France Recherche et Développement, Département Matériaux et Mécanique des Composants, Site des Renardières, Avenue des Renardières, Ecuelles, 77818 Moret sur Loing, France

An original approach is proposed to predict the behavior of the 16MND5 bainitic steel (similar to U.S. A508 cl.3) in the lower range of the ductile-to-brittle transition region and at lower temperatures [$-196\,°$C; $20\,°$C], by developing a new polycrystalline modeling concurrently with X-ray diffraction (XRD) analysis. A two-level homogenization is used to take into account each kind of heterogeneity as well as the phase and grain interactions. A Mori–Tanaka formulation first enables to describe the elastoplastic behavior of a bainitic single crystal (modeled as a single crystal ferritic matrix reinforced by cementite inclusions), while the transition to polycrystal is achieved by a self-consistent approach. This model can simulate in particular the effects of temperature. It reproduces qualitatively the stress distribution in the material (stress states are lower in ferrite than in the bulk material due to cementite particles, the difference never exceeding 150 MPa), the intergranular strain heterogeneity (ripples observed on the $\varepsilon_{\phi\psi} = f(\sin^2 \psi)$ curve) and the pole figures determined by XRD on different scales. The proposed approach is validated here on the macroscopic, phase and intraphase scale.

1. Introduction

Under normal service conditions, pressure vessel steels display a ductile behavior, but neutron irradiation ageing causes a temper embrittlement (low alloy 16MND5 or A508 steel [1,2]) which shifts their ductile-to-brittle transition range to higher temperatures. Therefore, to assess how the integrity of these steels may be compromised during a pressurized thermal shock (in case of an accident involving loss of coolant, for instance), it becomes necessary to consider their brittle behavior. It is thus very important to characterize the mechanical properties of such un-irradiated materials at very low temperatures [$-196\,°$C; $-60\,°$C] (especially the toughness and the mechanisms responsible for brittle fracture: nucleation and propagation of cracks) and to define relevant criteria [3,4], in order to predict their behavior and their service life.

Many models have been developed to simulate the evolution of behavior and fracture toughness in relation to temperature [5,6], but only a few apprehend materials as polycrystalline and/or heterogeneous ones, and they rarely reckon with the damaging processes or the effect of pre-notched specimens on stress concentration and crack tip plasticity (RKR conception models [7]). New approaches have therefore to be devised to take into consideration each kind of heterogeneity (especially on a crystallographic scale), and to determine the influence of microstructure on the macroscopic mechanical properties. These approaches require local fracture and damage criteria on the scale of the crystal lattice or the grain, which depend on the elastoplastic stress–strain history. The self-consistent models [8] including crystallographic gliding on slip systems, take into account the grain interactions and can predict the evolution of crystallographic textures [9] and internal stresses [10].

Multiphase material modeling has also been widely dealt with. Although the case of materials with different phase grains (two-phase austeno-ferritic steel [11] and multiscale modeling of titanium aluminides [12]) is relatively well-known, the modeling of the elastoplastic behavior of polycrystals containing intracrystalline precipitates is however more problematic, since the latter interact with the surrounding medium. The matrix may be reinforced with non-shearable particles so that the dislocations bypass them [13], leading to the formation of Orowan loops (globular pearlite [14], Al–Li alloys [15] and elastoplastic composites).

In this work, a polycrystalline model is developed concurrently with an experimental characterization of the 16MND5 bainitic steel (modeled as a ferritic matrix reinforced with cementite precipitates), in order to reproduce the behavior of the material at various
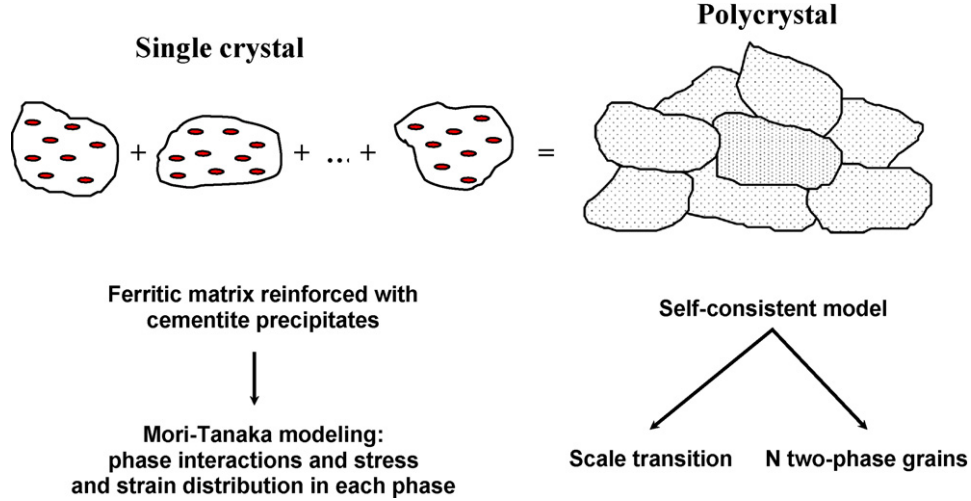
Fig. 1. Polycristalline modeling with a two-level homogenisation.

temperatures. It aims at predicting the stress states in each phase and the intergranular strain heterogeneity, all in relation to temperature. The problem is considered on a crystallographic scale, using a two-level homogenization; a Mori–Tanaka model is used to describe the behavior of a two-phase grain, while the transition to the polycrystal is achieved through an elastoplastic self-consistent approach (Fig. 1). With this type of microstructure, we consider that the crystallographic aspect and the mechanical response – anisotropic and different for each phase – take precedence over the morphological aspect.

Experimentally, the material response is obtained thanks to highly efficient tools. X-ray diffraction (XRD) is used because it is the only technique allowing the determination of the intergranular strains and the average stresses in each phase of the material. This technique is based on the measurement of the crystal lattice strains of each phase, from which one can deduce the respective average stress tensors thanks to the $\sin^2 \psi$-method [16]. For a given macroscopic strain path, the stress distribution enables us to understand the phenomena occurring in each phase of the material. All these measurements supply the model of behavior with data, enabling comparisons between numerical predictions and experiments, and ultimately providing grounds for the validation of said model.

For the sake of clear comprehension and legibility, this paper is divided into three parts. In the first one, the constitutive relations of a single crystal containing precipitates are presented, introducing a Mori–Tanaka formulation which takes into account phase interactions [17]. A parametrical study is then realized in order to analyze the influence of various parameters (volume fraction of precipitates, hardening parameters, critical resolved shear stress) on the stress distribution in a bainitic grain.

The second part is devoted to the polycrystalline modeling of the studied material (16MND5 bainitic steel). A self-consistent approach, similar to what has been proposed by Schmitt et al. [14] for hypo- and hyper-eutectoid steels, is developed to derive the polycrystal's overall behavior from the single crystal constitutive law previously obtained (first part). The per-phase average stresses and strains are thus deduced from the elastoplastic characteristics of each phase, as well as the volume fraction of precipitates and the distribution of the crystalline orientations in the polycrystal during loading and after unloading. A comparison with experimental data is also offered to illustrate (and criticize) the validity of the model produced.

Finally, in the third part, the intergranular strains and the average stress distribution in the material are discussed in relation to temperature. Here again, since the aim is to study for industrial pur-

poses the brittleness of the material and more especially cleavage, tensile tests and stress analyses by XRD are compared to simulated ones at various low temperatures and different scales.

2. Two-phase grain modeling

In the three scale polycrystalline approach proposed through this work, the lower scale is first considered. A Mori–Tanaka model is developed to describe the behavior of a two-phase body-centered cubic single crystal with a matrix/inclusion morphology. The small strain formalism is adopted because the considered material is tested and studied at low temperatures, which entails low macroscopic strains (characteristically between 3% and 10%).

2.1. Elastoplastic behavior of a single crystal

Plastic strain in a single crystal takes place when at least one slip system becomes active. A slip system g is first potentially active, if the resolved shear stress τ^g on the corresponding gliding plane reaches a critical value τ_c^g (Schmid's law):

$$\tau^g = \tau_c^g \tag{1}$$

with

$$\tau^g = R_{ij}^g . \sigma_{ij}. \tag{2}$$

σ_{ij} is the stress tensor, and the Schmid factors $R_{ij}^g = \frac{1}{2}(n_i^g \cdot m_j^g + n_j^g \cdot m_i^g)$ are related to the slip systems defined by the slip plane normal n^g and the slip direction m^g (Fig. 2).

Then, to be active, a slip system must also fulfill the consistency condition [18]:

$$\dot{\tau}_c^g - \dot{\tau}^g = 0. \tag{3}$$

The slip rate $\dot{\gamma}^g$ on each activated system g leads to the plastic strain rate:

$$\dot{\varepsilon}_{ij}^p = \sum_g R_{ij}^g \cdot \dot{\gamma}^g. \tag{4}$$

When considering a hardening matrix h^{gh} [19], a hardening rate $\dot{\tau}_c^g$ on slip system g can be formulated. It depends on the slip rate $\dot{\gamma}^h$

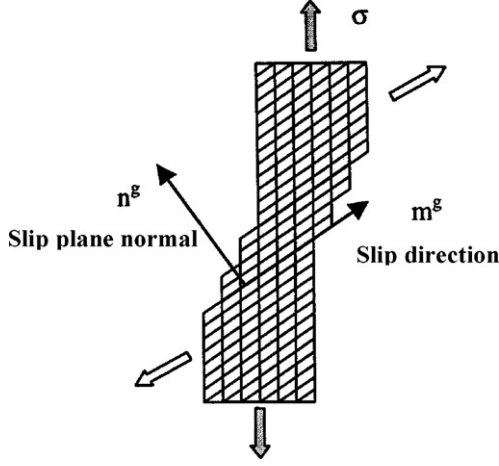$$\dot{\tau}_c^g = \sum_h h^{gh} \cdot \dot{\gamma}^h \tag{5}$$

Fig. 2. Definition of the crystallographic gliding.

where h^{gh} and τ_c^g are material parameters (this h^{gh} matrix describes the slip-systems interactions).

By adopting the small strain formalism, one has the constitutive relation of the single crystal from Hooke's law associated to the additive decomposition of the total strain rate in its elastic and plastic parts (respectively $\dot{\varepsilon}^e$ and $\dot{\varepsilon}^p$ (Eq. (7)))

$$\dot{\sigma}_{ij} = C_{ijkl} \cdot \dot{\varepsilon}_{kl}^e = C_{ijkl} \cdot (\dot{\varepsilon}_{kl}^t - \dot{\varepsilon}_{kl}^p) \tag{6}$$

where C_{ijkl} is the homogeneous elastic stiffness tensor and

$$\dot{\varepsilon}^t = \dot{\varepsilon}^e + \dot{\varepsilon}^p. \tag{7}$$

Eqs. (2), (4) and (6) are used to determine the relation

$$\dot{\tau}^g = R_{ij}^g \cdot C_{ijkl} \cdot \dot{\varepsilon}_{kl}^t - R_{ij}^g \cdot C_{ijkl} \cdot \sum_h R_{kl}^h \cdot \dot{\gamma}^h \tag{8}$$

so that the plasticity criterion (activation of potentially active slip systems (Eq. (3))) and Eq. (5) lead to

$$\sum_h H^{gh} \cdot \dot{\gamma}^h - R_{ij}^g \cdot C_{ijkl} \cdot \dot{\varepsilon}_{kl}^t = 0, \tag{9}$$

with

$$H^{gh} = h^{gh} + R_{ij}^g \cdot C_{ijkl} \cdot R_{kl}^h. \tag{10}$$

One can then deduce the energetic criterion of Franciosi and Zaoui [20], by summing only the potentially active slip systems

$$W = \frac{1}{2} \cdot \sum_h \sum_g H^{gh} \cdot \dot{\gamma}^h \cdot \dot{\gamma}^g - \sum_g R_{ij}^g \cdot C_{ijkl} \cdot \dot{\varepsilon}_{kl}^t \cdot \dot{\gamma}^g + D \tag{11}$$

where D is a constant.

All combinations of potentially active slip systems are tested; the unique, lowest combination, in terms of energy, will thus define the active slip systems. Other integration schemes and algorithms have also been proposed more recently, and their relative accuracy investigated [21]. Furthermore, some of them point out the influence of the elastic and plastic properties of the crystal [22].

From now on in this study, only the active slip systems g will be considered. For these systems, Schmid's law (3) and relation (5) give

$$\dot{\tau}_c^g = R_{ij}^g \dot{\sigma}_{ij} = \sum_h h^{gh} \cdot \dot{\gamma}^h. \tag{12}$$

Introducing Hooke's law and Eqs. (4) and (8) in the above relation, one has

$$R_{ij}^g \cdot C_{ijkl} \cdot \dot{\varepsilon}_{kl}^t = \sum_h (R_{ij}^g \cdot C_{ijkl} \cdot R_{kl}^h + h^{gh}) \cdot \dot{\gamma}^h \tag{13}$$

which leads to the expression of the slip rate $\dot{\gamma}^g$

$$\dot{\gamma}^g = \sum_h (R_{ij}^g \cdot C_{ijkl} \cdot R_{kl}^h + h^{gh})^{-1} \cdot R_{mn}^h \cdot C_{mnop} \cdot \dot{\varepsilon}_{op}^t. \tag{14}$$

Finally, from Eqs. (6) and (8), one obtains

$$\dot{\sigma}_{ij} = l_{ijkl} \cdot \dot{\varepsilon}_{kl}^t \tag{15}$$

where l is the elastoplastic tangent modulus the expression of which is

$$l_{ijkl} = \left(C_{ijkl} - \sum_g \sum_h C_{ijst} \cdot R_{st}^g \cdot \left(R_{mn}^g \cdot C_{mnop} \cdot R_{op}^h + h^{gh} \right)^{-1} \right.$$
$$\left. \cdot R_{qr}^h \cdot C_{qrkl} \right). \tag{16}$$

Therefore, l_{ijkl} depends on the elastic stiffness tensor C_{ijkl} of the single crystal, as well as on the orientation tensors R_{ij}^g, the set of active slip systems and the hardening parameters.

Furthermore, the orientation tensors depend on the Euler angles $\varphi_1, \varphi, \varphi_2$ [23] which characterize the crystal orientation in relation to the loading reference frame. After each strain increment, these angles are updated, just like the critical resolved shear stresses and l_{ijkl} (since the active slip system combination changes), and their evolution is given by Nesterova et al. [24]:

$$\begin{cases} \dot{\varphi}_1 = \left(\sin\varphi_2 \cdot \dot{\omega}_{23}^e + \cos\varphi_2 \cdot \dot{\omega}_{13}^e \right) / \sin\phi \\ \dot{\phi} = \dot{\omega}_{32}^e \cdot \cos\varphi_2 - \dot{\omega}_{13}^e \cdot \sin\varphi_2 \\ \dot{\varphi}_2 = \dot{\omega}_{21}^e - \left(\left(\sin\varphi_2 \cdot \dot{\omega}_{23}^e + \cos\varphi_2 \cdot \dot{\omega}_{13}^e \right) / \sin\phi \right) \cdot \cos\phi \end{cases} \tag{17}$$

where $\dot{\omega}_{ij}^e$ is the elastic rotation of the crystal lattice such as $\dot{\omega}_{ij}^e = -\dot{\omega}_{ij}^p$.

2.2. Single crystal with precipitates: Mori–Tanaka model

The Mori–Tanaka model enables to predict the stress and strain averages in a two-phase grain composed of a single crystal matrix (M) with a distribution of precipitates or inclusions (I). Hereafter, inclusions are considered to be exclusively elastic (elastic anisotropy) while the matrix plastic strain is induced by crystallographic gliding when slip systems become active (elastic and plastic anisotropy).

The elastic inclusion problem [25] gives the following relation between the average strain rate in the matrix and in the inclusions (respectively $\dot{\varepsilon}_M$ and $\dot{\varepsilon}_I$):

$$\dot{\varepsilon}_I = T \cdot \dot{\varepsilon}_M \tag{18}$$

where

$$T = [I + S^{Esh} \cdot C_M^{-1} \cdot (C_I - C_M)]^{-1} \tag{19}$$

takes into account the interactions between these two phases (the elastic moduli of the matrix and the inclusion are respectively denoted C_M and C_I). $I_{ijkl} = 1/2(\delta_{ik} \cdot \delta_{jl} + \delta_{il} \cdot \delta_{jk})$ is the unit tensor (δ_{ij} is the Kronecker symbol) and S^{Esh} the Eshelby tensor calculated from the Green tensor thanks to the Lebensohn and Tomé [26] method (anisotropic case, both Gauss and Jordan's techniques of numerical integration considering 2*72 integration points). This tensor depends on the elastic modulus of the matrix C_M and the shape of the inclusion.

Table 1
Elastic constants and parameters of the model considered for the bainitic grain.

Elastic constants (MPa)			Critical shear stress (MPa)	Hardening parameters (MPa)	
C_{11}	C_{12}	C_{44}	τ_c^g	h_1	$h_2 = 1.2 h_1$
237,400	134,700	116,400	100	100	120

To take into account the plastic flow throughout the matrix, the chosen C_M tensor is in fact the elastoplastic tangent modulus of the latter, so that

$$T = [I + S^{\text{Esh}} \cdot I_M^{-1} \cdot (C_I - I_M)]^{-1} \qquad (20)$$

with the Eshelby tensor calculated for the elastoplastic tangent modulus I_M.

Thus, considering the volume fraction f of inclusions and mixture rules, relation (18) leads to the localization of the strain rate in each phase

$$\dot{\varepsilon}_M = [(1-f) \cdot I + f \cdot T]^{-1} \cdot \dot{\varepsilon}^t \qquad (21)$$

$$\dot{\varepsilon}_I = T \cdot [(1-f) \cdot I + f \cdot T]^{-1} \cdot \dot{\varepsilon}^t \qquad (22)$$

from which one deduces

$$\dot{\sigma}_M = I_M \cdot \dot{\varepsilon}_M = I_M \cdot [(1 - f \cdot I + f \cdot T)]^{-1} \cdot \dot{\varepsilon}^t \qquad (23)$$

$$\dot{\sigma}_I = C_I \cdot \dot{\varepsilon}_I = C_I \cdot T \cdot [(1-f) \cdot I + f \cdot T]^{-1} \cdot \dot{\varepsilon}^t. \qquad (24)$$

$\dot{\sigma}^t$ and $\dot{\varepsilon}^t$ are respectively the overall stress and strain of the two-phase grain. Finally, from Eqs. (23) and (24), one can easily find:

$$\dot{\sigma}^t = (1-f) \cdot \dot{\sigma}_M + f \cdot \dot{\sigma}_I = [I_M + f \cdot (C_I \cdot T - I_M)]$$
$$\cdot [(1-f) \cdot I + f \cdot T]^{-1} \cdot \dot{\varepsilon}^t \qquad (25)$$

where $I_{M/I} = [I_M + f \cdot (C_I \cdot T - I_M)] \cdot [(1-f) \cdot I + f \cdot T]^{-1}$ is the two-phase elastoplastic tangent modulus [27,28].

It is worth emphasizing that Eq. (23) enables us to estimate the average stress history throughout the matrix which, in turn, allows us to derive the potentially active slip system. Furthermore, combinations of these potentially active slip systems define possible elastoplastic tangent moduli of the matrix I_M (right term of relation (20)). Thus, Eqs. (12), (16), (20) and (24) define a set of non-linear first-order differential equations whose unknowns are the stress average in the matrix, the active slip system combination (or the elastoplastic modulus), the critical resolved shear stresses and the Euler angles. This system is solved by an explicit integration method; after each overall strain increment, these internal variables are updated thanks to Eqs. (12), (16), (18) and (24).

In other words, this model enables to evaluate the overall stress rate response of a two-phase grain. When considering only spherical inclusions and elastic behaviors, it corresponds to the lower bound of the Hashin and Strikman [29] formulation.

2.3. Parametrical study of a bainitic grain during tensile tests

A bainitic grain (Fe/Fe_3C) is composed of a ferritic single crystal matrix (Fe) reinforced with cementite precipitates (Fe_3C inclusions), so that the Mori–Tanaka model defined in Section 2.2 leads to the relation

$$\dot{\sigma}^t = l_{Fe/Fe_3C} \cdot \dot{\varepsilon}^t = [l_{Fe} + f \cdot (C_{Fe_3C} \cdot T - l_{Fe})] \cdot [(1-f) \cdot I + f \cdot T]^{-1} \cdot \dot{\varepsilon}^t \qquad (26)$$

where the Eshelby tensor is calculated for the elastoplastic tangent modulus of ferrite I_{Fe} considering a spherical inclusion (the two point correlation functions of the ferrite and cementite phases are assumed to be isotropic). The crystallographic aspect is rather favored with the elastic anisotropy of the single crystal. During plastic deformation, the bainitic grain is submitted to the following overall elastoplastic strain rate $\dot{\varepsilon}^t$

$$\dot{\varepsilon}^t = \begin{pmatrix} 1 & 0 & 0 \\ 0 & -0.5 & 0 \\ 0 & 0 & -0.5 \end{pmatrix}. \qquad (27)$$

Slip is considered on $\{1\,1\,0\} \langle 1\,1\,1 \rangle$ and $\{2\,1\,1\} \langle 1\,1\,1 \rangle$ slip systems in ferrite, the behavior of which is defined by a critical resolved shear stress and a hardening matrix h^{gh} (reduced to two terms h_1 and h_2, respectively self-hardening and latent hardening [30]), while cementite is supposed to remain exclusively elastic.

The two phases (ferrite and cementite) have the same elastic constants [31]; they have been defined in Table 1 [32], as well as the hardening parameters h_1 and h_2 and the critical resolved shear stress τ_c^g (in ferrite). Under these conditions, a parametrical study permits us to determine the influence of the volume fraction of precipitates and of the initial shear stress on the overall behavior of the bainitic grain.

First, Fig. 3 gives the evolution of the stress (σ_{11} component) as a function of the macroscopic applied strain (ε_{11} component), when the volume fraction of cementite f varies, the orientation of the crystal being defined by three Euler angles ($\varphi_1 = 21$, $\phi_1 = 103°$, $\varphi_2 = 304°$ here). The model correctly shows that the overall stress and the hardening slope increase with the volume fraction of cementite, and also enables to compare the average stress in each phase (ferrite and cementite) with the bainite overall stress (ferritic matrix + cementite precipitates). As expected, the model indicates that the average stress in cementite is higher than the overall average, while it is lower in ferrite. This is explained by the mechanical property differences between the two phases, and in particular the yield stress, the bainitic grain being composed of a soft phase (ferritic matrix) and a hard phase (cementite precipitates). In the same way, the stresses in each phase and the overall hardening slope all increase with the volume fraction of cementite f. Incidentally, the difference between the stress in ferrite and the one in bainite follows the same evolution, since ferrite accommodates most of the applied total strain. In Fig. 4, one can notice that cementite saturates above a certain strain rate as well; it almost stops gathering strain (strain which is then accommodated by ferrite). This result may seem surprising at first, because this figure represents
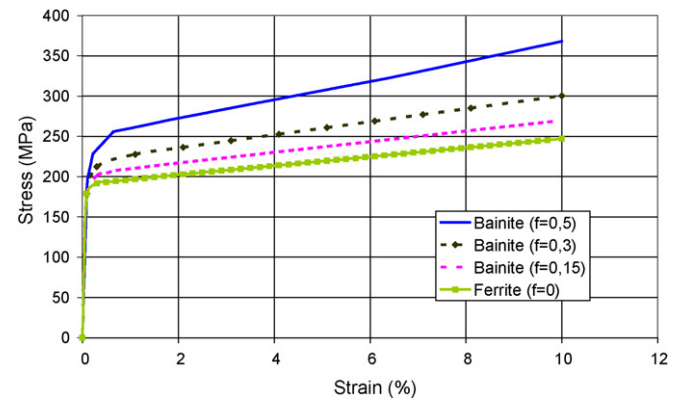

Fig. 3. Influence of the volume fraction of cementite (f) on the bainitic single crystal overall strain-stress behavior (Mori-Tanaka model).
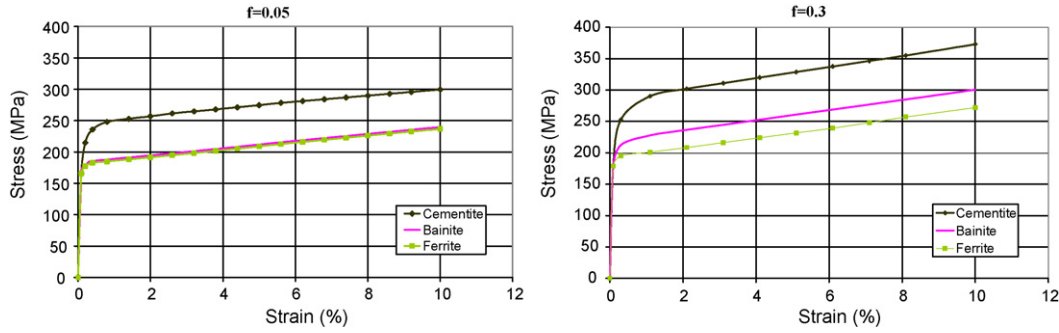
Fig. 4. Influence of the volume fraction of cementite on the stress distribution (σ_{11} component) in a bainitic single crystal (Mori-Tanaka model): predicted overall average stress as well as stress averages in ferrite and cementite phases are plotted as a function of the overall strain (ε_{11} component).
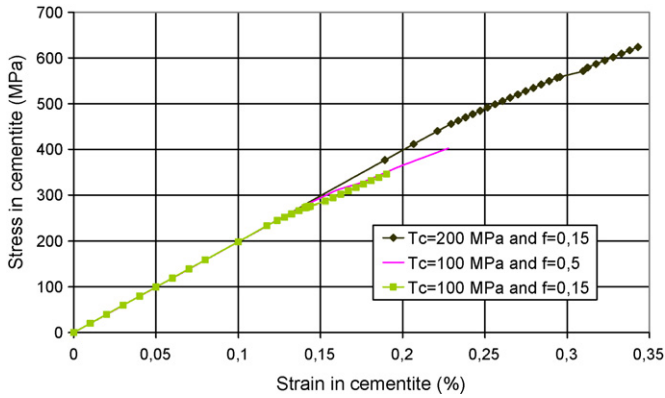

Fig. 5. Average stress (σ_{11} component) in cementite (Mori-Tanaka model: bainitic single crystal) as a function of the average strain in cementite (ε_{11} component): influence of the initial value of the critical resolved shear stress (Tc) and the volume fraction of cementite (f).

Fig. 7. Influence of the initial value of the critical resolved shear stress (100 and 200 MPa) on the stress distribution (σ_{11} component) in a bainitic single crystal (Mori-Tanaka model, f = 0.15): predicted overall average stress as well as stress averages in ferrite and cementite phases are plotted as a function of the overall strain (ε_{11} component).

the stress in each phase as a function of the applied macroscopic strain, but the evolution of stress in cementite as a function of the strain in cementite (and not of the macroscopic strain anymore (Fig. 5)) confirms that this phase does remain perfectly elastic (note that this figure also gives us the opportunity to analyze the influence of the critical resolved shear stress; σ_{Fe_3C} and ε_{Fe_3C} are proportional to the latter and increase with the volume fraction f as well). So in fact, there is a stress and strain distribution in each phase of the bainitic grain (ferrite and cementite). This is a particularity of the Mori–Tanaka model, which takes into account the matrix–precipitates interactions on the scale of the grain. For
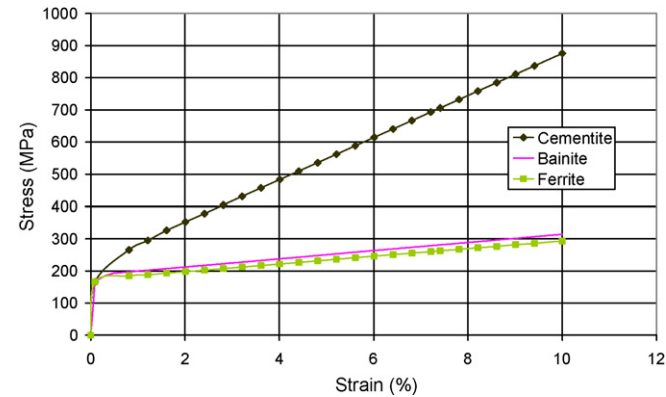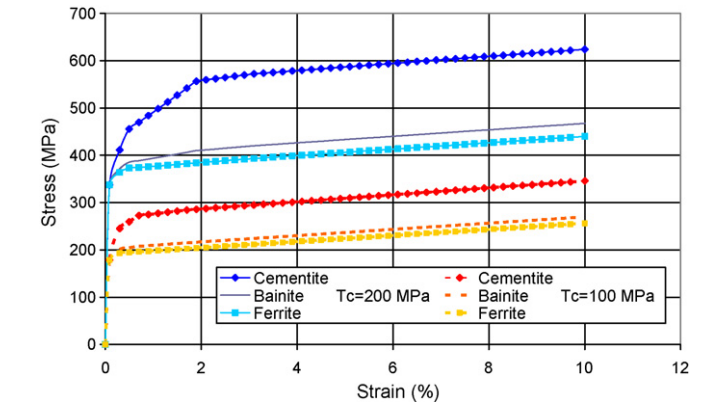

Fig. 6. Stress distribution (σ_{11} component) in a bainitic single crystal using a self-consistent model (f=0.15): predicted overall average stress as well as stress averages in ferrite and cementite phases are plotted as a function of the overall strain (ε_{11} component).

example, the self-consistent model (see Section 3) applied to the same bainitic grain gives a different evolution for cementite (considering the same material parameters), since the stress states in this phase are much higher (Fig. 6). The influence of the initial value of the critical resolved shear stress is given by Fig. 7; the yield stress and the stress difference between each phase increase with it.

Since crystalline plasticity on the grain scale is correctly modeled, the next section is devoted to the 16MND5 polycrystalline steel. A self-consistent approach is combined with such calculations in order to obtain the macroscopic behavior of this material from the crystallographic mechanisms in each grain.

3. Polycrystalline 16MND5 bainitic steel

3.1. Presentation of the studied material

The material considered is a 16MND5 bainitic pressure vessel steel (similar to U.S. A508 cl.3) used in pressurized water reactors; its chemical composition is given in Table 2. It has undergone sev-

Table 2
Chemical composition of the 16MND5 bainitic steel (weight percentage, iron balance).

C	S	P	Mn	Si	Ni	Cr	Mo
0.159	0.008	0.005	1.37	0.24	0.70	0.17	0.50

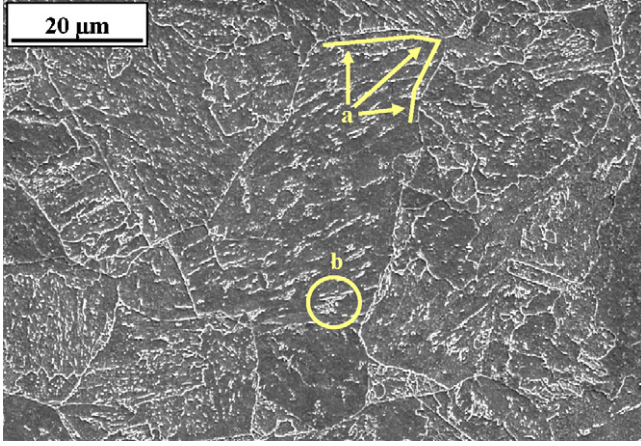| V	Cu	Co	Al	N	O [ppm]	Sn [ppm]	As [ppm]
<0.01	0.06	<0.01	0.023	0.007	35–36	50	160

Fig. 8. SEM micrograph showing the microstructure of the 16MND5 steel (a) Former austenitic grain boundaries (b) Ferrite with cementite precipitates.

Fig. 9. Unloading as modeled for the bainitic grain: the same unloading stress σ^u is removed from the last average stress in each phase.

eral heat treatments: two austenizations followed by water quench, a tempering and a stress-relief treatment. The resulting microstructure is a tempered bainite one (Fig. 8). The prior austenitic grains are composed of a ferritic matrix containing many carbides, mainly under the form of cementite precipitates, as cementite needles (in superior bainite) or as cementite spheres (in inferior bainite); their characteristic dimension is of the order of 0.3 μm. The volume fraction of cementite considered in this paper is about 5%. It has been estimated using picture correlation techniques, but energy dispersal diffraction and neutron diffraction measurements will be soon realized for a precise quantification (the volume fraction will probably be a little lower). No initial texture is present, which has been verified using XRD (pole figures with intensity ratios inferior to 3).

A series of sequenced and in situ tensile tests is performed concurrently with the polycrystalline modeling in order to characterize the mechanical properties of this steel. Several specimens are broken at various low temperatures, reached by using a liquid nitrogen cooler. Each test consists in a succession of loading and unloading leading to the failure of the material. At each step, XRD is used to determine the average elastic strain in ferrite and the stress distribution throughout the material. It shows in particular that one phase is in compression (ferrite) while the other is in tension (cementite) after unloading.

3.2. Polycrystalline modeling: self-consistent approach

This polycrystalline material is considered as an aggregate of perfectly bonded bainitic single crystals which differ by their Euler angles. In this instance, the self-consistent approach is adopted in order to derive its macroscopic mechanical behavior from the crystallographic strain mechanisms on the scale of the grain. For elastoplastic materials, the macroscopic constitutive relation reads

$$\dot{\Sigma} = L_{\text{eff}} \cdot \dot{E}^t, \tag{28}$$

where L_{eff} is the macroscopic elastoplastic tangent modulus, and $\dot{E}^t$ and $\dot{\Sigma}$ the macroscopic strain and stress rates, respectively.

Furthermore, the average total strain rate for the grains of same crystallographic orientation $\dot{\varepsilon}_{ij}(\Omega)$ can be calculated by Hill [33]

$$\dot{\varepsilon}_{ij}(\Omega) = \left[I_{ijkl} + S_{ijkl}^{\text{Esh}} \cdot L_{ijkl}^{-1} \cdot (l_{ijkl}(\Omega) - L_{ijkl}) \right]^{-1} \cdot \dot{E}_{kl}^t, \tag{29}$$

where Ω is one grain orientation characterized by the three Euler angles, $l_{ijkl}(\Omega)$ the two-phase elastoplastic tangent modulus of the considered grain (Eq. (25)) and S_{ijkl}^{Esh} the Eshelby tensor calculated for L_{ijkl}.
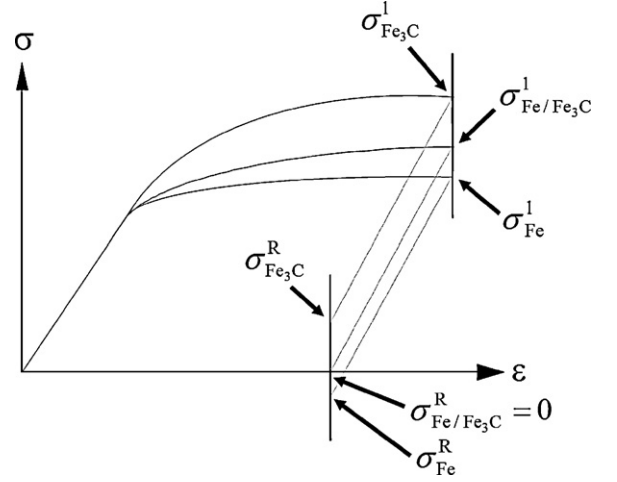
Using the local behavior law for each grain

$$\dot{\sigma}_{ij} = l_{ijkl} \cdot \dot{\varepsilon}_{kl} \tag{30}$$

and the stress average relation

$$\dot{\Sigma}_{ij} = \overline{\dot{\sigma}_{ij}(\Omega)} \tag{31}$$

one can finally deduce the constitutive relation for the polycrystal (Eq. (28)), where

$$L_{\text{eff}} = L_{ijkl} = \overline{l_{ijkl}(\Omega) \cdot \left[I_{ijkl} + S_{ijkl}^{\text{Esh}} \cdot L_{ijkl}^{-1} \cdot (l_{ijkl}(\Omega) - L_{ijkl}) \right]^{-1}} \tag{32}$$

This last equation defines implicitly the macroscopic elastoplastic modulus; it is resolved by the use of a fixed-point iterative procedure [14]. When considering the 16MND5 steel, this equation can be written as

$$L_{\text{Fe/Fe}_3\text{C}} = \overline{l_{\text{Fe/Fe}_3\text{C}}(\Omega) \cdot \left[I + S^{\text{Esh}} \cdot L_{\text{Fe/Fe}_3\text{C}}^{-1} \cdot (l_{\text{Fe/Fe}_3\text{C}}(\Omega) - L_{\text{Fe/Fe}_3\text{C}}) \right]^{-1}} \tag{33}$$

with $L_{\text{Fe/Fe}_3\text{C}}$ the macroscopic elastoplastic modulus and $l_{\text{Fe/Fe}_3\text{C}}(\Omega)$ the elastoplastic moduli of the different bainitic single crystals.

A macroscopic elastic unloading is also introduced in the model (the elastoplastic moduli of the single crystals are reduced to elastic ones in that case), so that comparisons can be made, especially with the XRD experimental measurements. Thus, the average residual stress in each bainitic grain after unloading $\sigma_{\text{Fe/Fe}_3\text{C}}^r(\Omega)$ is determined from the last average stress in the grain during loading $\sigma_{\text{Fe/Fe}_3\text{C}}^r(\Omega)$ and the same "unloading stress" (Fig. 9):

$$\sigma_{\text{Fe/Fe}_3\text{C}}^r(\Omega) = \sigma_{\text{Fe/Fe}_3\text{C}}^l(\Omega) - \sigma^u(\Omega) \tag{34}$$

Thus, the resulting average macroscopic stress is accordingly zero, but not all the grains return to a zero stress.

The micromechanical problem being elastically homogeneous (each phase has the same elastic constant)

$$c_{\text{Fe/Fe}_3\text{C}} = c_{\text{Fe}} = c_{\text{Fe}_3\text{C}} = c(\Omega) \tag{35}$$

the overall elastic modulus is calculated from

$$C_{\text{Fe/Fe}_3\text{C}}^l = \overline{c(\Omega) \cdot \left[I + S^{\text{Esh}} \cdot C_{\text{Fe/Fe}_3\text{C}}^{l-1} \cdot (c(\Omega) - C_{\text{Fe/Fe}_3\text{C}}^l) \right]^{-1}} \tag{36}$$

and the unloading stress reads

$$\sigma^u(\Omega) = c(\Omega) \cdot \varepsilon^u(\Omega) = c(\Omega) \cdot \left[I + S^{\text{Esh}} \cdot C_{\text{Fe/Fe}_3\text{C}}^{u-1} \cdot (c(\Omega) - C_{\text{Fe/Fe}_3\text{C}}^u) \right]^{-1} \cdot E^u$$
$$= c(\Omega) \cdot \left[I + S^{\text{Esh}} \cdot C_{\text{Fe/Fe}_3\text{C}}^{l-1} \cdot (c(\Omega) - C_{\text{Fe/Fe}_3\text{C}}^l) \right]^{-1} \cdot C_{\text{Fe/Fe}_3\text{C}}^{l-1} \cdot \Sigma^l \tag{37}$$

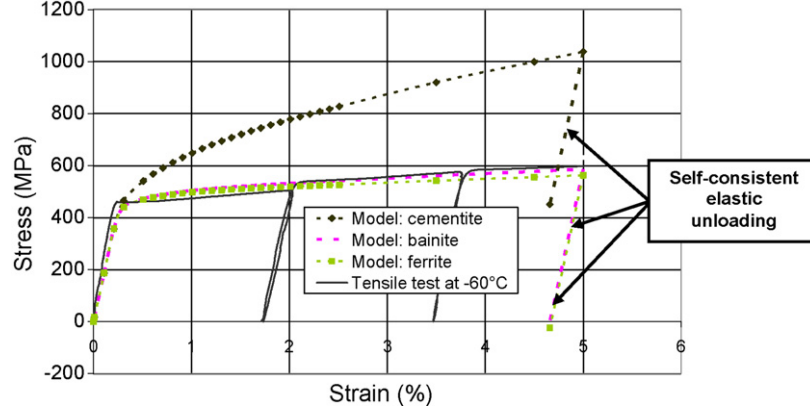| Elastic constants (MPa)			Critical shear stress (MPa)	Hardening parameters (MPa)	
C_{11}	C_{12}	C_{44}	τ_c^g	h_1	$h_2 = 1.2h_1$
237,400	134,700	116,400	230	220	264

Fig. 10. Tensile test at $-60°$C on the 16MND5 steel. Experimental results (overall stress-strain curve) are compared to simulated ones; average stresses in cementite and ferrite are also reported.

where the Eshelby tensor S^{Esh} is calculated for the overall elastic modulus, and E^u and Σ^1 are respectively the unloading macroscopic strain and the last overall macroscopic stress before unloading.

As a result, ferrite and cementite are considered to be unloaded in the same way (self-consistent scheme)

$$\begin{cases} \sigma_{Fe}^r(\Omega) = \sigma_{Fe}^l(\Omega) - \sigma^u(\Omega) \\ \sigma_{Fe_3C}^r(\Omega) = \sigma_{Fe_3C}^l(\Omega) - \sigma^u(\Omega) \end{cases} \tag{38}$$

3.3. Simulation of the behavior of the 16MND5 steel

To apply the self-consistent approach to the 16MND5 bainitic steel, one thousand grains are considered (each one is defined as a two-phase grain (part II)), the crystallographic orientations of which are chosen at random, so that no initial crystallographic texture is present (however, a given texture can be introduced on demand into the model, for example if needed for the material). Several simulations of the polycrystal behavior are thus realized, considering the same test parameters as in Section 2.3. To compare with the experimental tensile tests, this time the calculations have been performed using the tensor:

$$\dot{\sigma}^t = \begin{pmatrix} 1 & 0 & 0 \\ 0 & 0 & 0 \\ 0 & 0 & 0 \end{pmatrix}. \tag{39}$$

An interesting aspect of this model is that only four parameters need to be adapted in order to reproduce exactly the experimental results: the volume fraction of cementite (equal to $f = 0.05$ for the studied steel), the critical resolved shear stress τ_c^g (which takes into account the precipitate hardening and has an influence on the yield stress), as well as h_1 and h_2. For example, in the case of a tensile test at $-60°$C (Fig. 10), they have all been identified as presented in Table 3.

The developed polycrystalline model is also able to predict the evolution of crystallographic textures, which is corroborated for instance by the 30% and 100% total strain simulated pole figures in Fig. 11 (classical textures obtained for BCC materials submitted to tensile tests [23]). These pole figures are close to the 16MND5 experimental one obtained after a tensile test at $-60°$C, using XRD (Fig. 12). Admittedly, the texture is not exactly the same, but that is simply because failure takes place at this temperature after only 9.5% total strain (meaning that the texture has not completely developed yet).

Since the model permits the calculation of the stress in each phase during loading and after unloading (Fig. 13), a direct comparison can be done with the values determined by XRD. This technique is used because it is the only one that enables to determine the average stress in each phase ($\sin^2 \psi$ method) and for each crystallographic orientation, i.e. each grain. A small in situ tensile machine
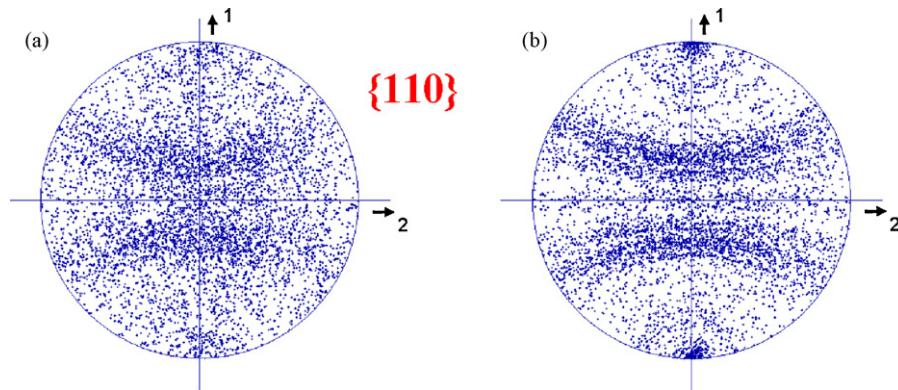

Fig. 11. {110} Pole figures corresponding to a tensile test (aggregate of 1000 grains chosen with no initial texture) (a) 30% strain (b) 100% strain.
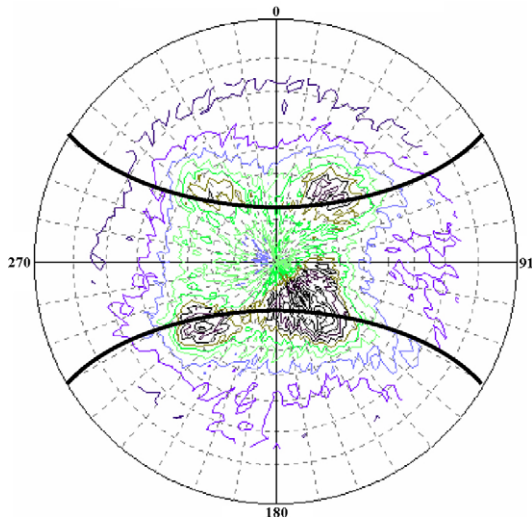
Fig. 12. {220} experimental pole figure corresponding to a tensile test at −60°C (9.5% strain).
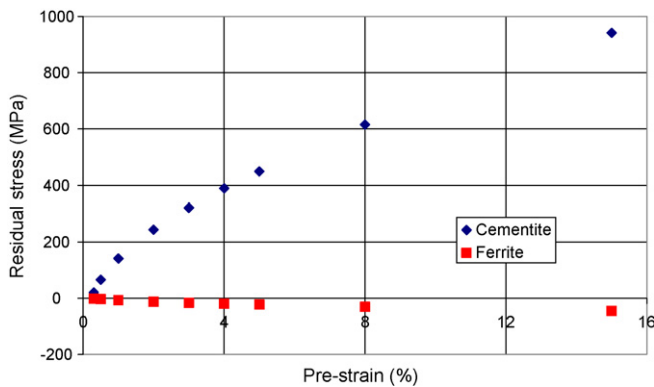

Fig. 13. Evolution of the simulated residual average stress (σ_{11}^r component after complete unloading) in ferrite and cementite as a function of the macroscopic tensile strain in the 16MND5 steel (−60°C).
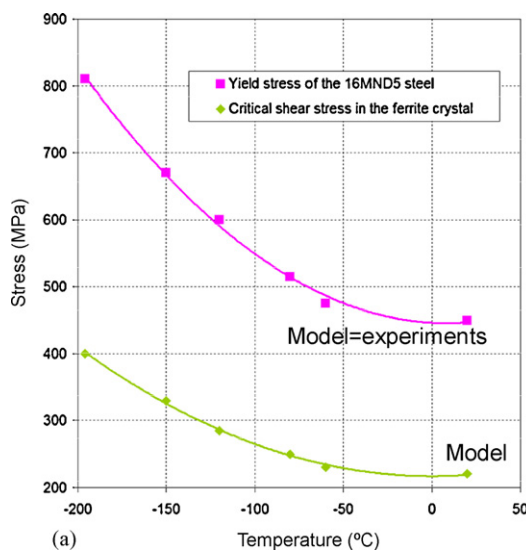
Table 4
Evolution of the average stress in ferrite with the overall strain: XRD results are compared to simulated ones at -60°C (16MND5 steel).

Overall strain (%)	6.5	11.9
XRD measurements (MPa)	−80 ± 20	−105 ± 30
Simulated results (MPa)	−28	−45

is placed directly on a diffraction goniometer so that measurements can be realized throughout the tensile tests (60 mm long specimens), during loading, at the last point of loading, and after unloading, with the temperature remaining constant all through the proceedings. The stress analyses are conducted in ferrite while the values of the internal stresses in cementite are deduced by using a mixture law, since the volume fraction of this phase is too small for direct measures. These unique experiments have been validated at low temperatures [−160°C; −60°C], and one can notice that after unloading, while the residual average macroscopic stress $\Sigma_{\text{Fe/Fe}_3\text{C}}^r$ is reduced to zero, the difference observed between the average stress in each phase before unloading is maintained; cementite is effectively in tension ($\Sigma_{\text{Fe}_3\text{C}}^r > 0$), and ferrite in compression ($\Sigma_{\text{Fe}}^r < 0$). This corresponds to the results obtained from XRD measurements in ferrite: −80(±20) MPa and −105(±30) MPa for pre-strain of respectively 6.5% and 11.9% (the volume fraction of cementite being too small, no measures can be taken, so the stress in this phase is deduced using a classical mixture rule). Thus, the observed difference between the macroscopic stress and the average stress in ferrite increases with the applied strain without exceeding 105 MPa; it can be greater in other materials such as duplex steel (>200 MPa [34]) or pearlitic steels (>400 MPa [35]). However, if the stress states in each phase are well predicted by the model, this difference is still a little underestimated (only 45 MPa: see Table 4). This point will be discussed in the next part.

4. Temperature effects and intergranular strains

All the tensile tests carried out at different temperatures have shown that the slopes of the macroscopic stress–strain curves are linear and similar in the elastic and the plastic parts. With a hardening first considered as constant (no parameter to identify), the effects of temperature can be therefore introduced into the model by identifying only the initial value of the critical resolved shear stress τ_c^g parameter for each temperature (it is the only
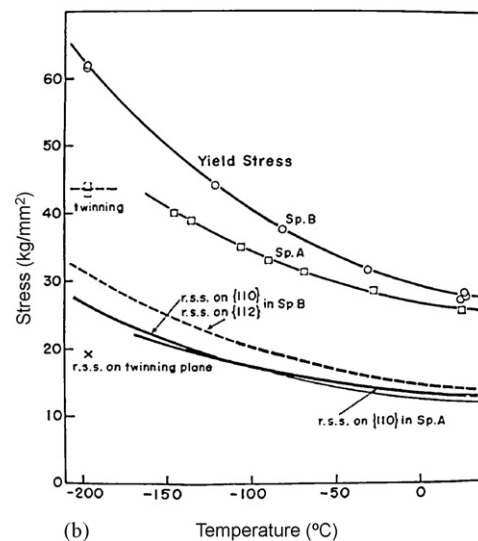

Fig. 14. Evolution with temperature of the yield stress and the initial value of the critical resolved shear stress in the ferrite crystal τ_c^g (which has been identified with experiments from −196°C to room temperature): (a) 16MND5 steel (b) Fe-3% single crystal alloy (Taoka et al., 1964).

Temperature (°C)	−196	−150	−120	−80	−60	20
Initial value of the critical resolved shear stress in the ferritic phase (MPa)	400	330	285	250	230	220
Yield stress of the 16MND5 steel (MPa)	810	670	600	515	475	450

temperature-dependent parameter; its variation in ferrite from −196 °C to 20 °C is given in Fig. 14 and Table 5) so that the predicted yield stress of the material corresponds to the experimental one (the former is reported on the same figure). The obtained results, here compared to other authors' works, show that their evolution is not linear. As expected, the initial value of the critical resolved shear stress is higher at low temperatures since the yield stress and the stress states in the material are then more important. In agreement with the tensile tests performed at temperatures ranging from −196 °C to −60 °C, it afterwards decreases as temperature increases and tends to a horizontal asymptote ($\tau_c^g = 200$ MPa), as the yield stress does. These results are reproduced without appreciable change for different sets of initial crystallographic orientations chosen at random. The temperature related variations of the critical resolved shear stress are similar to those obtained in Fe–3%Si alloys by Qiao and Argon [36]) and especially Taoka et al. [37], with precisely the same curve shape, even though the values of τ_c^g are lower in such alloys because they are composed of large single crystals and do not contain any hard phase such as cementite to raise the yield stress as in the 16MND5 bainitic steel (Orowan loops stored around it). Moreover, our values can be compared to those identified at room temperature by M'Cirdi et al. [38] in the ferrite grain of a duplex steel (grain by grain XRD stress analysis): $\tau_c^g = 170$ MPa for a non-aged material and $\tau_c^g = 250$ MPa in the case of an aged one, the yield stress of which is higher. The yield stress/critical resolved shear stress ratio is also comparable to the one predicted by our model, since it remains rather close to two. However, the critical resolved shear stress evolution of the two slip system families $\{1\,1\,2\}\langle1\,1\,1\rangle$ and $\{1\,1\,0\}\langle1\,1\,1\rangle$ is not considered separately in our paper, because there is very little difference between the two except at extremely low temperatures; the distinction will be made in future works.

The proposed modeling can therefore predict the evolution with temperature of the per-phase average stress distribution in the material. The stress is higher in cementite, the behavior of which is always elastic, while the stress in ferrite remains close to that in bainite ($\sigma_{Fe_3C} > \sigma_{Fe/Fe_3C} > \sigma_{Fe}$), whatever the temperature considered (Figs. 10 and 15). Furthermore, the difference between the macroscopic stress and the average stress in ferrite increases with the applied strain and also with decreasing temperatures. This numerical result is consistent with the experimentally observed one (XRD measurements) which show that at −150 °C for example (Fig. 15), ferrite does not go beyond 700 MPa (3.6% strain) while cementite reaches values the order of 2600 MPa, and that
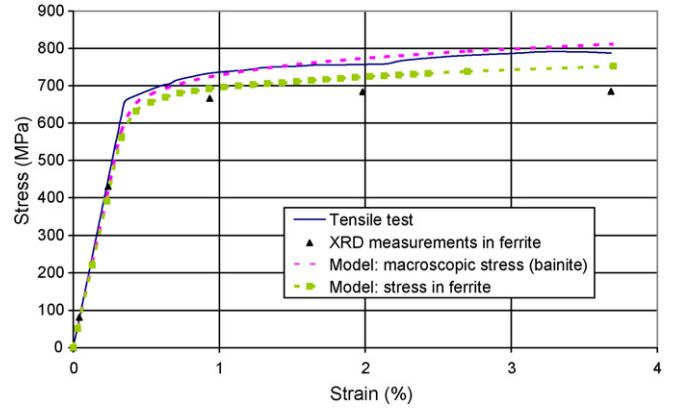

Fig. 15. Overall stress-strain curve during a tensile test at −150°C on the 16MND5 steel: experimental results are compared to simulated ones (the stress in cementite is deliberately not represented in this figure for better readability).

the residual stress in ferrite is maximum (−150 MPa) at −196 °C (the difference between bainite and ferrite being again underestimated by the model (almost 100 MPa)). These high stress values in cementite are not excessive – they will be soon confirmed by direct in situ measurements at low temperatures using synchrotron emission –, since other authors like Belassel [35] and Martinez-Perez et al. [39] for instance, have already determined similar ones in pearlitic steels (respectively around 2400 MPa and 1700 MPa), using synchrotron radiation.

XRD is also used to measure the $\varepsilon_{\phi\psi} = f(\sin^2 \psi)$ intergranular strains in several $\phi\psi$ directions in the ferritic phase of the material [40]. $\varepsilon_{\phi\psi}$ is the strain in the direction of the normal to the $\{h\,k\,l\}$ planes

$$\varepsilon_{\phi\psi} = \frac{d - d_0}{d_0} = \frac{\sin\theta_0}{\sin\theta_\phi} - 1 \approx -\frac{1}{2}.\text{cotan}\theta_0 \cdot \Delta 2\theta_\phi \qquad (40)$$

where d_0 and θ_0 are respectively the lattice spacing and the Bragg angle corresponding to a stress free state.

The lattice strains express the variation of the interreticular distance d due to stress, with the ψ angle characterizing the crystallographic orientation of the grains. Thus, considering the $\{2\,1\,1\}$ planes in the tensile direction ($\phi=0°$), the results show that the average slope is negative after unloading because it is linked to the compressive state of ferrite (Fig. 16a). The $\sin^2 \psi$ relation is not linear as for isotropic materials, but shows semicircular ripples, which
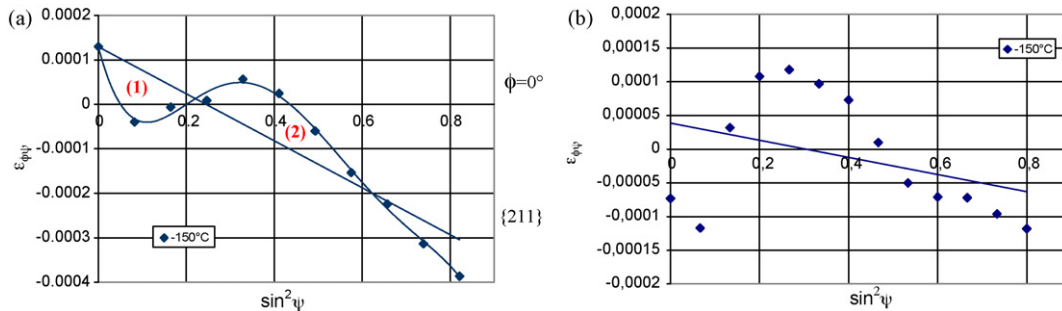

Fig. 16. $\varepsilon_{\phi\psi} = f\left(\sin^2 \psi\right)$ intergranular strains at −150°C (4% macroscopic strain, after unloading) (a) XRD results (b) Polycrystalline modeling.
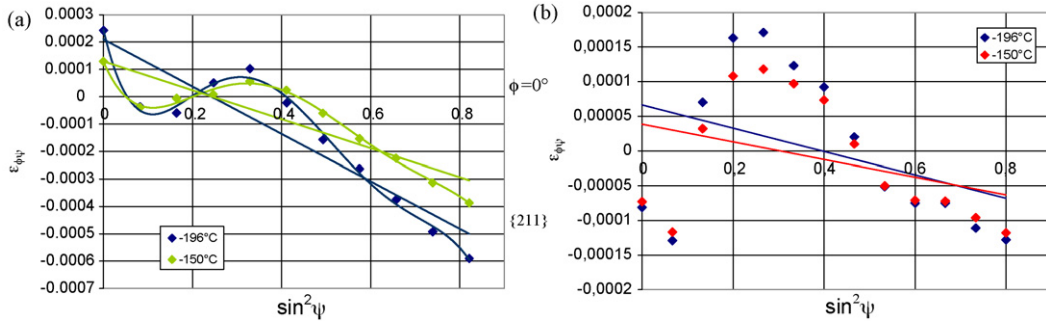
Fig. 17. influence of temperature on the $\varepsilon_{\phi\psi} = f\left(\sin^2\psi\right)$ intergranular strains (4% macroscopic strain, after unloading) (a) XRD results (b) Polycrystalline modeling.

are very interesting because they are usually only observed in materials which have a crystallographic texture. In fact, they characterize the heterogeneity of the elastic strain (the deviations to the average slope are related to the anisotropic character of the local strain (order II: intergranular strain)), which leads to a different mechanical response for each crystal orientation. The intergranular stresses in the ferritic phase are therefore different according to the crystallographic orientation of the grains considered [34]; some grains are less strained (1) or more strained (2) than the macroscopic average (Fig. 16a).

These $\varepsilon_{\phi\psi} = f(\sin^2\psi)$ intergranular strains can also be calculated with the proposed modeling (Fig. 16b), by projecting the elastic strain tensor normally to the diffracting plane considered

$$\varepsilon_{\phi\psi} = \left\langle n_i \cdot \varepsilon_{ij}^e \cdot n_j \right\rangle_{\phi,\psi} \tag{41}$$

In these conditions, the model reproduces the same ripples as the ones experimentally observed—they are well predicted. It confirms that intergranular strains and stresses are emphasized at low temperatures, due to the increasing of yield stress (Fig. 17). The grains undergo a stronger loading (the strain levels and the average stress in ferrite are higher) and the heterogeneities related to their orientation are enhanced, which makes the accommodation of strain by ferrite for each crystallographic orientation more difficult. This correctly predicted temperature dependence is a valuable feature of the model. The real asset of this highly efficient model is therefore the fact that, contrary to most models, not only does it come experimentally validated on the macroscopic scale, but also on a lower one (phase and intraphase!).

Having said this, the calculated strain values deviate slightly from those measured by XRD (they are lower: see Fig. 16b), the same way as the average stress in each phase, because the stress in ferrite is still a little underestimated. Indeed, if the slope of the curve was steeper, that is to say if the residual stress in the ferritic phase was higher, one would notice that the strain levels predicted by the model would consequently adjust to agree with experimental ones. This could probably be improved by taking now into account a non-linear kinematic hardening depending on temperature or dislocations densities, which would give lower critical resolved shear stresses and therefore more accurate stress states. The representation of the bainitic microstructure could also be made more relevant and more accurate by introducing a new distribution of the volume fraction of cementite (within bounds of the 5% constant for the whole material), like Qiu and Weng [41] for example. This is all the more necessary as EBSD measurements have shown that each grain is in fact composed of several packets, with their own crystallographic orientation. These packets, which can be purely ferritic or reinforced with cementite particles (bainitic packets), define the material's real characteristic microstructural length and can be, therefore, considered as the "effective" grains in the model. For example, when considering the material as a polycrystalline aggregate of not only just perfectly bonded bainitic grains, but both pure ferritic and bainitic grains (the latter presenting a higher local cementite volume fraction (33%)), the first simulations already give a higher stress difference (20 MPa more: Fig. 18) between ferrite and the macroscopic value, much closer to the XRD results.
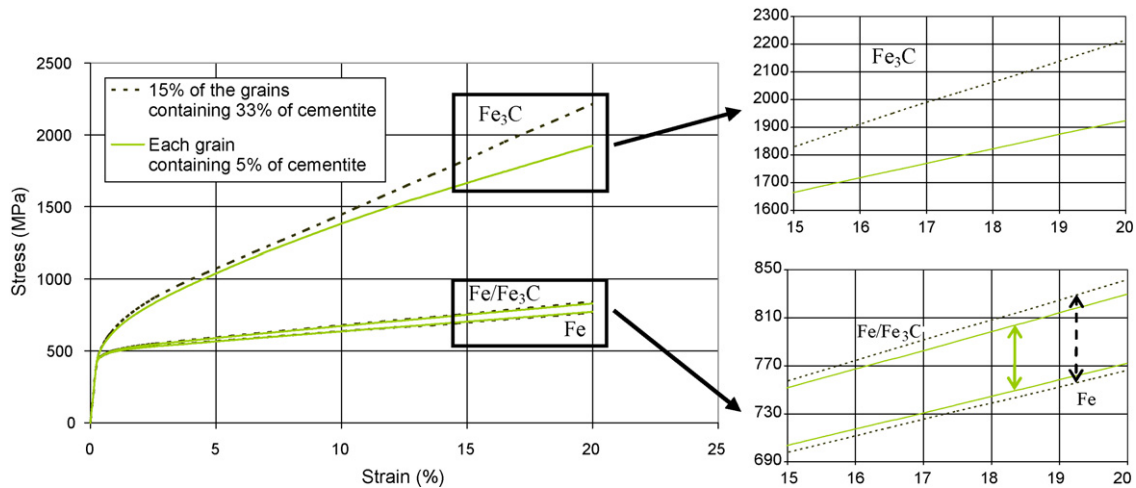

Fig. 18. comparison between two simulations during a tensile test at $-60°$C on the 16MND5 steel. The resulting stress difference between each phase is higher when the material is composed of both pure ferritic grains and bainitic grains (the global volume fraction of cementite remains constant: 5%).

5. Conclusions

The polycrystalline Mori–Tanaka/self-consistent modeling here developed is very efficient and well adapted to the 16MND5 bainitic steel, because it correctly represents the microstructure of this material (an aggregate of randomly oriented bainitic grains) and is able to predict the evolution of its elastoplastic behavior in relation to temperature, from $-150\,°C$ to room temperature. Indeed, the stress difference between ferrite and bainite remains inferior to $150\,MPa$ ($\sigma_{Fe} < \sigma_{Bainite} < \sigma_{Fe_3C}$, as determined by XRD) and the $\varepsilon_{\phi\psi} = f(\sin^2\psi)$ strains in ferrite are qualitatively in agreement with the experimental XRD results. The influence of the volume fraction of cementite and of the initial crystallographic texture on the stress distribution in the material can also be determined.

This model is therefore validated at different scales (macroscopic, phase and intraphase) with efficient experimental tools (especially using XRD), but it could be still further improved to derive average stress levels in the ferritic phase that would be quantitatively consistent with XRD measurements. The last simulations mentioned in part IV, in particular, display significant improvements simply by considering the material as an aggregate of both ferritic and bainitic grains. The volume fraction of cementite must be determined precisely especially using neutron diffraction rather 2 or 3%?), because it has a great influence on the level of stress predicted in this phase. Furthermore, since self-consistent modeling only considers average quantities (and not the continuity of phase properties), one can imagine using the finite element method to obtain numerical solutions for strain and stress fields as well (one-scale analysis [42] and 2D problems [43]). This would be all the more interesting as it would permit to take into account the intragranular heterogeneities observed by coupling Electron Back-Scattered Diffraction (EBSD) with Kossel microdiffraction (diffraction within a SEM which enables to associate in situ microstructure observations with determined strain/stress states on the micron scale [44]). This point will be developed in future works. Alternatively, the effects of non-linear kinematic hardening as well as critical resolved shear stress differences between $\{1\,1\,2\}\langle1\,1\,1\rangle$ and $\{1\,1\,0\}\langle1\,1\,1\rangle$ slip system families will also be studied. Once this constitutive law re-formulated, the modeling of fracture properties of the 16MND5 steel will finally be addressed [45]. This will require many in situ tests (SEM, EBSD, XRD) at various temperatures and from multiaxial, non-proportional loading, in order to understand all the fracture mechanisms taking place directly during loading between $-196\,°C$ and $-60\,°C$ (influence of the loading path change too), and to provide crystallographic damage criteria (especially for cleavage initiation and propagation).

Acknowledgements

References

[1] D.M. Parks, J. Eng. Mat. Tech. 98 (1976) 30–36.
[2] M. Al Mundheri, P. Soulat, A. Pineau, Proceedings of the International Seminar on Local Approach of Fracture, Moret-sur-Loing, 1986, pp. 243–256.
[3] T. Narström, M. Isacsson, Mat. Sci. Eng. A 271 (1999) 224–231.
[4] M. Mäntylä, R. Rossoll, I. Nebdal, C. Prioul, B. Marini, J. Nucl. Mat. 264 (1999) 257–262.
[5] K. Wallin, Defect Assessment in Components—Fundamentals and Applications ESIS/EGF9, Mechanical Engineering Publications, London, 1991, pp. 415–445.
[6] X. Gao, G. Zhang, T.S. Srivatsan, Mat. Sci. Eng. A 415 (2006) 264–272.
[7] R.O. Ritchie, J.F. Knott, J.R. Rice, J. Mech. Phys. Sol. 21 (1973) 395–410.
[8] R. Hill, J. Mech. Phys. Sol. 13 (1965) 89–101.
[9] R.A. Lebensohn, G.R. Canova, Acta Mater. 45 (1997) 3687–3694.
[10] R. Masson, M. Bornert, P. Suquet, A. Zaoui, J. Mech. Phys. Sol. 48 (2000) 1203–1227.
[11] A. Baczmánski, C. Braham, Acta Mater. 52 (2004) 1133–1142.
[12] A. Roos, J.L. Chaboche, L. Gélébart, J. Crépin, Int. J. Plast. 20 (2004) 811–830.
[13] N. Bonfoh, A. Carmasol, P. Lipinski, Int. J. Plast. 19 (2003) 1167–1193.
[14] C. Schmitt, P. Lipinski, M. Berveiller, Int. J. Plast. 13 (1997) 183–199.
[15] R. Monzen, H. Mizutani, Mat. Sci. Eng. A 231 (1997) 105–110.
[16] V. Hauk, Structural and Residual Stress Analysis by Nondestructive Methods, Elsevier Science B.V., Amsterdam, 1997, pp. 132–215.
[17] T. Mori, K. Tanaka, Acta Metal. 21 (1973) 571–574.
[18] J.W. Hutchinson, Proceedings of the Royal Society of London A 319, 1970, pp. 247–272.
[19] R. Hill, J. Mech. Phys. Sol. 14 (1966) 95–102.
[20] P. Franciosi, A. Zaoui, Int. J. Plast. 7 (1991) 295–311.
[21] E.P. Busso, G. Cailletaud, Int. J. Plast. 21 (2005) 2212–2231.
[22] R.D. McGinty, D.L. McDowell, Int. J. Plast. 22 (2006) 996–1025.
[23] H.J. Bunge, Texture Analysis in Materials Science—Mathematical Methods, Butterworths Publishers, London, 1982.
[24] E.V. Nesterova, B. Bacroix, C. Teodosiu, Metal. Mat. Trans. A 32A (2001) 2527–2538.
[25] J.D. Eshelby, Proceedings of the Royal Society of London A 241, 1957, pp. 376–396.
[26] R.A. Lebensohn, C.N. Tomé, Acta Metal. Mat. 41 (1993) 2611–2624.
[27] Y. Benveniste, Mech. Mat. 6 (1987) 147–157.
[28] J. Schjødt-Thomsen, R. Pyrz, Mech. Mat. 33 (2001) 531–544.
[29] Z. Hashin, S. Strikman, J. Mech. Phys. Sol. 10 (1963) 343–352.
[30] P. Franciosi, M. Berveiller, A. Zaoui, Acta Metal. 28 (1980) 273–283.
[31] B.M. Drapkin, B.V. Fokin, Phys. Met. Metal. 49 (1980) 177–183.
[32] W.F. Hosford, The Mechanics of Crystals and Textured Polycrystals, Oxford University Press, New York, 1993.
[33] R. Hill, J. Mech. Phys. Sol. 13 (1965) 213–222.
[34] K. Inal, J.L. Lebrun, M. Belassel, Metal. Mat. Trans. A 35A (2004) 2361–2369.
[35] M. Belassel, Etude de la distribution des contraintes d'ordre I et II par diffraction des rayons X dans un acier perlitique, PhD Thesis, Ecole Nationale Supérieure d'Arts et Métiers de Paris, France, 1994.
[36] Y. Qiao, A.S. Argon, Mech. Mat. 35 (2003) 313–331.
[37] T. Taoka, S. Takeuchi, E. Furubayashi, J. Phys. Soc. Jpn. 19 (1964) 701–711.
[38] L. M'Cirdi, J.L. Lebrun, K. Inal, G. Barbier, Acta Mater. (2001) 3879–3887.
[39] M.L. Martinez-Perez, F.J. Mompean, J. Ruiz-Hervias, C.R. Borlado, J.M. Atienza, M. Garcia-Hernandez, M. Elices, J. Gil-Sevillano, R.L. Peng, T. Buslaps, Acta Mater. 52 (2004) 5303–5313.
[40] K. Inal, P. Gergaud, M. François, J.L. Lebrun, Scand. J. Metal. 8 (1999) 139–150.
[41] Y.P. Qiu, G.J. Weng, Mech. Mat. 12 (1991) 1–15.
[42] J.M. Mathieu, M. Berveiller, K. Inal, O. Diard, Fat. Frac. Eng. Mat. Struct. 29 (2006) 725–737.
[43] M. Kovač, L. Cizelj, Nucl. Eng. Des. 235 (2005) 1939–1950.
[44] R. Pesci, M. Berveiller, K. Inal, E. Patoor, J.L. Lecomte, A. Eberhardt, Mat. Sci. For. 524–525 (2006) 109–114.
[45] B. Tanguy, C. Bouchet, S. Bugat, J. Besson, Eng. Frac. Mech. 73 (2006) 191–206.